Non-Darcy Porous-Media Flow According to the Barree and Conway Model: Laboratory and Numerical-Modeling Studies

Bitao Lai, Jennifer L. Miskimins, and **Yu-Shu Wu,** SPE, Colorado School of Mines

Summary

This paper presents the results of our new experimental studies conducted for high flow rates through proppant packs, which show that the Barree and Conway (2004) flow model is capable of overcoming limitations of the Forchheimer non-Darcy equation at very high flow rates. To quantify the non-Darcy flow behavior using the Barree and Conway model, a numerical model is developed to simulate non-Darcy flow. In addition, an analytical solution is presented for steady-state linear non-Darcy flow and is used to verify the numerical-simulation results. The numerical model incorporates the Barree and Conway model into a general-purpose reservoir simulator for modeling multidimensional, single-phase non-Darcy flow in porous and fractured media and supplements the laboratory findings. The numerical model is then used to perform sensitivity analysis of the Barree and Conway flow model's parameters and to investigate transient behavior of non-Darcy flow at an injection well.

Introduction

The objectives of this paper are (1) to present experimental data from our current laboratory studies of high flow rates through proppant packs and (2) develop mathematical-modeling tools to quantify such high-flow-velocity, non-Darcy-flow behavior. Our experimental results show that non-Darcy flow occurs at high flow rates and that the conventional Forchheimer model may not be sufficient to describe the observed high-flow-rate behavior. On the other hand, the Barree and Conway (2004) flow model is found to be able to match the entire range of observed data from low to high flow rates. The modeling tools developed include both analytical and numerical approaches for simulating single-phase non-Darcy flow with the Barree and Conway model. In addition, the numerical model is used to perform parameter-sensitivity analysis and to obtain insight into transient non-Darcy flow with the Barree and Conway flow model.

Darcy's law (Darcy 1856) is the foundation for studies of fluid flow in porous media. According to Darcy's law, the pressure gradient ($\partial P/\partial L$) can be related to the fluid viscosity μ and superficial velocity v through a constant k (permeability), as demonstrated in Eq. 1:

$$-\frac{\partial P}{\partial L}=\frac{\mu v}{k}. \qquad (1)$$

Forchheimer (1901) observed deviations from the linearity of Darcy's Law at high flow rates. Forchheimer expanded Darcy's linear form into a quadratic flow equation that is now commonly referred to as Forchheimer's equation (Eq. 2):

$$-\frac{\partial P}{\partial L}=\frac{\mu v}{k}+\beta\rho v^2. \qquad (2)$$

This paper (SPE 122611) was accepted for presentation at the SPE Rocky Mountain Petroleum Technology Conference, Denver, 14–16 April 2009, and revised for publication. Original manuscript received for review 20 February 2009. Revised manuscript received for review 16 February 2011. Paper peer approved 10 March 2011.

Even with this additional quadratic term, Eq. 2 may not adequately describe all of Forchheimer's data; therefore, he eventually added an additional cubic term (Eq. 3) to try to account for these deviations. Other authors have also noted the inability of Forchheimer's equations to describe all data sets (Carmen 1937; Fand et al. 1987; Kececioglu and Jiang 1994; Montillet 2004; Barree and Conway 2004). The effect of these discrepancies can have a major impact on the assessment of flow rate or pressure distribution for a given porous medium, as shown in **Fig. 1** (a typical Forchheimer plot, in which "X"-axis is $\rho v/\mu$, and "Y"-axis is $\frac{dP}{dL}=\frac{1}{\mu v}$). Fig. 1 shows an example of experimental data that deviates from the Forchheimer plot. Fig. 1 also shows that β is not a constant with increased flow rate.

$$-\frac{\partial P}{\partial L}=\frac{\mu v}{k}+\beta\rho v^2+\gamma\rho v^3, \qquad (3)$$

where β = non-Darcy coefficient, 1/m; and ρ = fluid density, kg/m^3.

Jones (1972) specifically noted that large deviation from the linear Forchheimer plot occured for core samples with large values of the term βk_d. He shows that the Forchheimer plot becomes concave downward, leading to the observation of higher apparent permeability than those predicted by Forchheimer's equation at high velocity. Also, at higher velocity, the β-factor denoted for inertial force is not a constant for porous media.

Based on extensive experimental results and field observations, Barree and Conway (2004) proposed a new, more general model for non-Darcy flow in porous media that does not rely on the assumptions of a constant permeability or a constant β-factor. In their model, Darcy's law is still assumed to apply, but the absolute permeability is replaced by the apparent permeability, shown in Eq. 4:

$$-\frac{\partial P}{\partial L}=\frac{\mu v}{k_{\mathrm{app}}}, \qquad (4)$$

where k_{app} is the apparent permeability and is defined as

$$k_{\mathrm{app}}=k_{\min}+\frac{(k_d-k_{\min})}{(1+N_{\mathrm{Re}})^E}. \qquad (5)$$

Eq. 4, along with Eq. 5, is called the Barree and Conway flow model in this paper. In Eq. 5, k_{app} becomes constant (plateau behavior) at low (i.e., k_d) and high Reynolds numbers (N_{Re}). The plateau behavior at low Reynolds numbers was experimentally validated by several authors (i.e., Fand et al. 1987) before Barree and Conway (2004). On the other hand, the plateau behavior at high Reynolds numbers is a hypothesis, and it is partly validated by Lopez (2007) and Lai (2010). The exponential coefficient E in Eq. 5 describes the overall heterogeneity of the test samples. Its relation with sorting of a porous medium is examined by Lai (2010). The better the sorting, the closer the value of E is to 1.0. For single-sieve proppant (the proppants remain in the specified sieve in a sieve-analysis experiment), the value of E is equal to

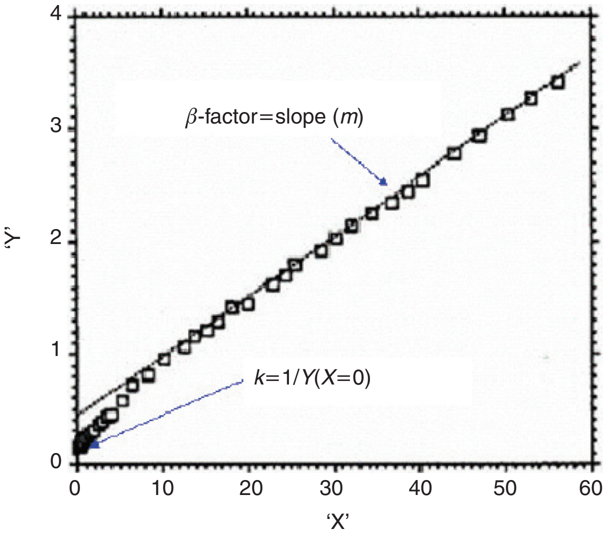

Fig. 1—Typical Forchheimer plot where the β-factor is the slope of the line and the permeability (k) is the intercept. Note that the changing slope of the data indicates that the β-factor is not a constant in porous media, based on the experimental data (Martins et al. 1990).

1.0. Therefore, it can be deduced that for a homogeneous porous medium, the value of E is equal to unity. In this work, for the proppant packs tested, which can be considered homogeneous, E is found to be equal to unity (Barree and Conway 2004; Lai 2010). In Eq. 5, N_{Re} is defined by

$$N_{\mathrm{Re}} = \frac{\rho v}{\mu \overline{\tau}},$$

where k_{app} = apparent rate-dependent permeability, k_{min} = minimum permeability at high rate, k_d = constant Darcy permeability, N_{Re} = Reynolds number, ρ = density, g/cm^3, v = superficial velocity, cm/s, μ = viscosity, and $\overline{\tau}$ = inverse of the characteristic length.

The dimensionless form of Eq. 5, when the E equals unity, can be written as Eq. 6:

$$\eta = \frac{k_{app}}{k_d} = \frac{k_{min}}{k_d} + \frac{1 - \dfrac{k_{min}}{k_d}}{\left(1 + N_{\mathrm{Re}}\right)}. \quad \text{(6)}$$

In Eqs. 5 and 6, $\overline{\tau}$, inverse of the characteristic length, is related to the mean particle size (Barree and Conway 2004). Also, $\overline{\tau}$ is correlated to the closure stress and the crushing and failure of the proppant grains.

There are several advantages to, or benefits of, using the Barree and Conway equation. First, it provides a single equation to describe the entire range of flow velocities through porous media tested. This is of great benefit to quantitative or modeling studies because a single equation can be programmed to model flow without needing to artificially set switchover points from Darcy- to non-Darcy-flow regimes. Second, because the equation describes the entire range of flow velocities, physical-transition zones are also honored and captured as flow velocities increase or decrease. The model also provides for a plateau area or a constant apparent permeability at high rates, which has been suggested and modeled by other authors (Ergun 1952; Fand et al. 1987). In particular, our experimental data show that the equation developed by Barree and Conway is able to overcome many of the drawbacks that numerous authors have pointed out when conducting Forchheimer analysis while still honoring the basics of Darcy and Forchheimer flow behavior under lower flow rates.

Laboratory Experimental Data and Results

A large number of experiments with proppant packs have been carried out using a single-phase nitrogen non-Darcy-flow apparatus developed by Lopez (2007). The apparatus uses a cell system consisting of a 20-cm-long Tygon tube (to account for embedment) with an inlet diameter of 0.95 cm. The cell is filled with proppant and five pressure ports, spaced 5 cm apart, which are installed along the pack (see **Fig. 2**). The assembled proppant pack is placed in a high-pressure vessel that can apply various closure stresses from 0–34.5 MPa using a hydraulic oil system. The inlet gas-flow rate ranges from 0–105 g/sec, which covers most gas-production rates encountered in the field. Note that the gas-flow rate in this work is three times higher than the flow rate in Barree and Conway (2004) (the highest N_{Re} in this paper is 320, while the highest N_{Re} in Barree and Conway's work is approximately 100).

As an example, the procedure of the test is illustrated under 136-atm (2,000-psi) confining-stress conditions. First, a 136-atm (2,000-psi) confining stress is applied to the test sample by a hydraulic oil pump. When the confining stress is stable, nitrogen gas with a purity greater than 99% is injected into the proppant pack, with an inlet gas pressure of 122.5 atm (1,800 psi). When the gas-flow rate reaches steady-state conditions, the five port pressures, temperature inside the proppant pack, and the gas mass-flow rate are recorded by a data-aquistion system. When the data correction is finished, the inlet-gas pressure is lowered to 109 atm (1,600 psi) while keeping the confining stress constant, and nitrogen gas continues to be injected into the proppant pack. The port pressures, the temperature, and mass-flow rate of gas are then again recorded. This procedure is repeated until the gas-inlet pressure reaches the lower limit (for instance, 6.8 atm or 100 psi). Proppant samples tested to date include a wide range of commonly used sizes and types, including ceramics and natural sands, ranging from 12/16 to 100 mesh. Experimental data are analyzed using a regression method for the Forchheimer quadratic and cubic methods and the Barree

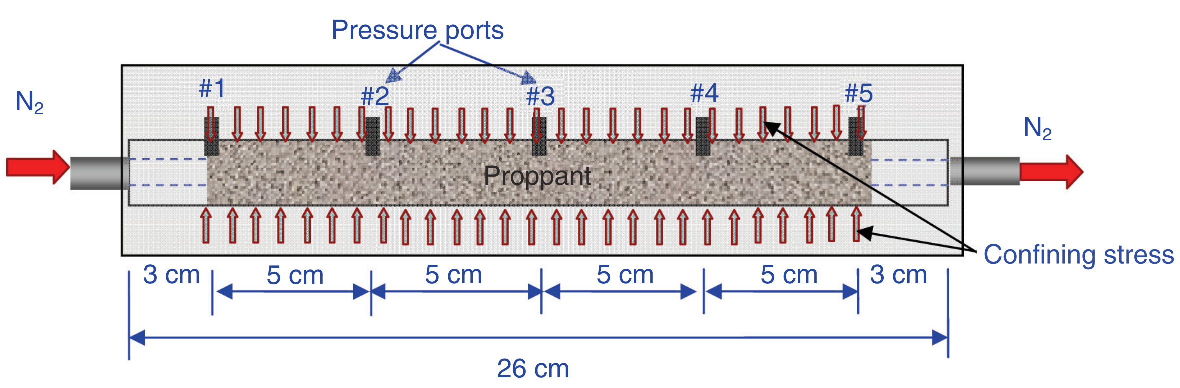

Fig. 2—Schematic of the proppant pack used in the non-Darcy-flow test system. Proppant is placed in a 20-cm-long Tygon tube with an inlet diameter of 0.95 cm. Five pressure ports are installed along the pack with a spacing of 5 cm, which provides a pressure profile across the pack, not just at the inlet and outlet. Confining stresses are applied to the pack using hydraulic oil.

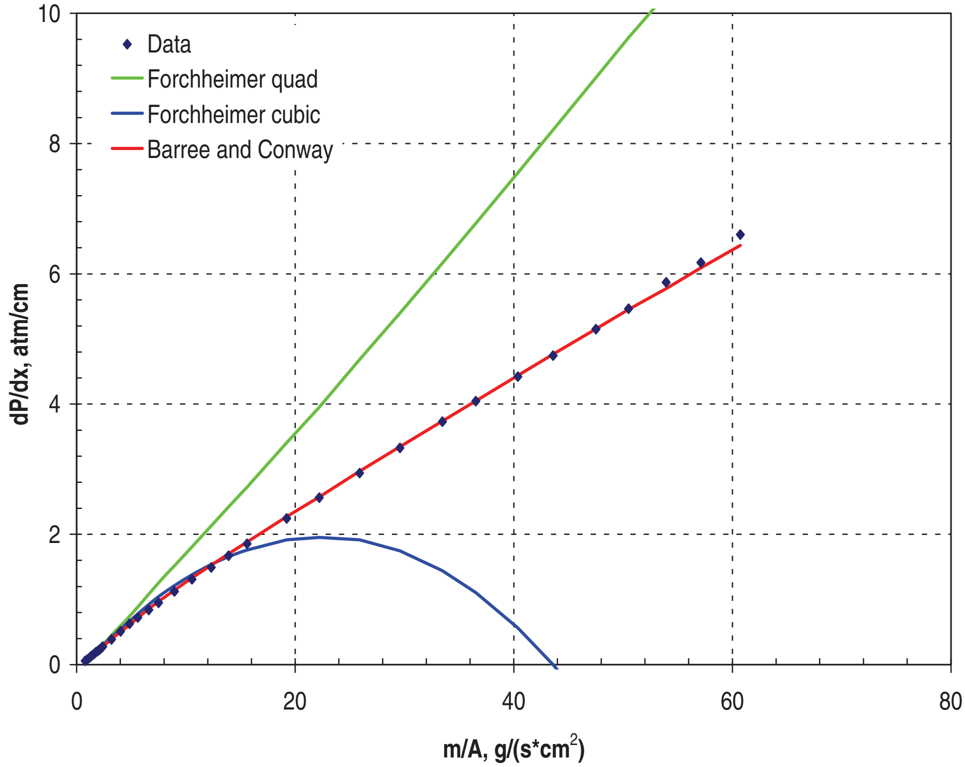

Fig. 3—Results of pressure gradient vs. mass-flow rate for a ceramic 20/40 proppant under a confining stress of 27.5 MPa. The experimental data (blue diamonds) agree with the Barree and Conway model (red) from low to high flow rates. The Forchheimer quadratic correlation (green) overestimates the pressure drop, while the Forchheimer cubic correlation (blue) underestimates the pressure drop at high gas-flow rates.

and Conway technique (Eqs. 2 through 4). Because continuous and significant variations of pressure-gradient and gas-property parameters are expected along the pack, all calculations and analyses are performed at the midpoint of the pack. The pressure gradient of the midpoint of the cell is calculated using the numerical-differentiation technique known as central-difference-derivative formulae (Griffiths and Smith 2006), as follows:

$$\left.\frac{\mathrm{d}P}{\mathrm{d}L}\right|_{P3} = \frac{1}{12h}(P_1 - 8P_2 + 8P_4 - P_5)$$

where $\frac{dP}{dL}$ = pressure gradient at the midpoint of the cell, P_1 = pressure at Port 1, P_2 = pressure at Port 2, P_3 = pressure at Port 3, P_4 = pressure at Port 4, P_5 = pressure at Port 5, and h = distance between each port.

A detailed explanation regarding how to conduct the data reduction is provided in Lopez (2007). An example showing the comparison among the experimental results and the three flow models is shown in **Fig. 3,** where the x-axis is normalized for mass-flow rate instead of fluid velocity. The data plotted in Fig. 3 are taken from a ceramic 20/40 proppant under a confining stress (cp) of 27.5 MPa (4,000 psig). The experimental data obtained from the laboratory tests are tabulated in **Table 1.** The gas mass-flow rate ($\dot{m}$) measurement in these experiments is based on the real-gas law (Lopez 2007), for which a known-volume gas tank is used. The key parameters in each flow model (for instance, β-factor in the Forchheimer quadratic equation; γ in the Forchheimer cubic equation; and $k_{\min}$, $k_{\min}/k_d$, and $\overline{\tau}$ in the Barree and Conway model) are obtained by using the back-regression analysis (curve-fitting) technique. In Table 1, P_1 through P_5 represent the different ports (see Fig. 2) at which pressure values are measured during the experiments; P_{ti} and T_{ti} are the initial pressure and temperature in the gas tank, respectively; and P_{tf} and T_{tf} are the final pressure and temperature in the gas tank, respectively. The field units in the measurement will be converted to SI units in the calculation.

As can be seen in Fig. 3, the experimental data agree quite well with the Barree and Conway model across the entire flow-velocity range from low to high gas-flow rates. The Forchheimer quadratic correlation overestimates the associated pressure drop, and the Forchheimer cubic equation deviates from the experimental data at high gas-flow rate. All sample data taken to date show similar agreement with the Barree and Conway equation across the observed flow spectrum.

Fig. 4 is a summary plot of all the test data taken to date using the dimensionless form of the Barree and Conway model (Eq. 6). Fig. 4 demonstrates that all of the experimental data collapse into one curve in agreement with the Barree and Conway model, as would be expected in a dimensionless form. One plateau of the log-dose equation format is clearly observed at low Reynolds numbers. When converted to field units, the test data shown in Fig. 4 cover field gas-production rates from less than 707.2 m^3/d to more than 283 168 m^3/d, demonstrating that the model is accurate across the intervals of interest for the industry.

Mathematical Model

In order to complement the laboratory-data results and quantify non-Darcy-flow behavior in reservoirs, numerical and analytical modeling is needed in general. We consider an isothermal reservoir system consisting of one single-phase fluid (gas or liquid) in porous or fractured media.

Governing Equation. In an isothermal system containing one fluid, one mass-balance equation is needed to describe the fluid flow in porous media and mass conservation of the fluid, leading to Eq. 7:

$$\frac{\partial}{\partial t}(\phi\,\rho) = -\nabla \bullet (\rho \mathbf{v}) + q, \quad \text{.......................... (7)}$$

where ϕ is the effective porosity of the medium, ρ is the density of the fluid under reservoir conditions, q is the sink/source term of the phase per unit volume of formation, and $\mathbf{v}$ is the superficial-flow-velocity vector, defined in the following (Eq. 8), an extended Barree and Conway's model in a vector form for multidimensional flow:

TABLE 1—EXPERIMENTAL DATA OBTAINED FROM THE CERAMIC 20/40 PROPPANT-PACK TESTS UNDER A CONFINING STRESS OF 4,000 psi (27.5 MPa)

Test	P_1 (psig)	P_2 (psig)	P_3 (psig)	P_4 (psig)	P_5 (psig)	T (°F)	P_{ti} (psig)	T_{ti} (°F)	P_{tf} (psig)	T_{tf} (°F)	Δt (s)	$\frac{dP}{dx}$ (atm/cm)	m/A (gm/s-cm^2)
1	110	104	100	95	90	73.0	0.0	72.5	4.3	76.1	30	0.056	0.80
2	120	112	106	99	91	73.0	0.0	72.6	5.3	76.0	30	0.080	0.99
3	131	122	114	104	93	73.0	0.0	72.4	6.6	76.5	30	0.109	1.21
4	140	129	119	108	94	73.0	0.0	72.1	7.4	76.9	30	0.134	1.37
5	151	137	126	112	95	73.0	0.0	71.1	8.4	76.8	30	0.159	1.56
6	161	146	132	116	96	73.0	0.0	71.1	9.4	76.2	30	0.185	1.74
7	171	154	139	120	97	73.0	0.0	71.1	10.3	76.3	30	0.205	1.91
8	181	162	145	125	98	72.9	0.0	70.7	11.3	76.8	30	0.230	2.09
9	191	170	151	129	100	72.9	0.0	71.0	12.1	77.0	30	0.252	2.25
10	200	178	157	137	101	72.9	0.0	73.6	12.8	77.8	30	0.276	2.39
11	247	216	188	154	106	72.7	0.0	69.3	17.2	76.0	30	0.387	3.20
12	298	259	222	229	112	72.7	0.0	68.7	21.6	76.5	30	0.509	4.01
13	353	305	259	226	120	72.7	0.0	66.9	26.0	76.5	30	0.625	4.84
14	396	341	288	236	126	72.7	0.0	65.6	30.2	76.9	30	0.721	5.60
15	454	390	329	278	134	72.6	0.0	68.0	35.3	75.5	30	0.840	6.60
16	507	436	366	374	144	72.6	0.0	64.8	40.2	76.1	30	0.949	7.49
17	597	513	431	427	165	72.5	0.0	62.7	48.1	76.6	30	1.120	8.95
18	697	598	502	403	193	72.5	0.0	61.5	56.8	77.2	30	1.307	10.56
19	804	690	580	458	226	72.4	0.0	61.9	66.2	76.7	30	1.493	12.32
20	899	773	650	629	256	72.3	0.0	65.2	74.5	76.3	30	1.672	13.90
21	1004	863	727	639	288	72.3	0.0	63.1	83.7	77.1	30	1.856	15.59
22	1216	1047	882	729	353	72.3	0.0	63.5	102.7	76.4	30	2.245	19.21
23	1396	1202	1014	817	409	72.3	0.0	68.8	118.5	77.1	30	2.564	22.20
24	1603	1381	1165	936	472	72.2	0.0	63.2	138.2	77.1	30	2.940	25.90
25	1816	1565	1321	1029	538	72.2	0.0	65.3	157.6	77.6	30	3.325	29.58
26	2038	1757	1483	1203	607	72.2	0.0	66.7	177.8	77.4	30	3.729	33.46
27	2211	1908	1611	1258	661	72.1	0.0	64.6	193.8	77.4	30	4.044	36.53
28	2427	2096	1771	1446	730	72.1	0.0	62.3	214.5	78.6	30	4.422	40.37
29	2608	2254	1905	1756	787	72.1	0.0	65.6	231.0	77.8	30	4.745	43.61
30	2832	2449	2071	1908	857	72.1	0.0	69.2	251.5	77.8	30	5.149	47.53
31	3003	2599	2198	2060	911	72.1	0.0	62.6	267.5	77.9	30	5.461	50.51
32	3222	2789	2357	1852	977	72.1	0.0	71.0	286.1	78.4	30	5.869	53.95
33	3398	2947	2494	2183	1037	72.1	0.0	63.2	303.1	77.4	30	6.173	57.12
34	3626	3148	2663	2087	1103	72.1	0.0	63.2	323.4	77.4	30	6.600	60.73

$$-\nabla\Phi = \frac{\mu \mathbf{v}}{k_d\left(k_{mr} + \dfrac{\left(1-k_{mr}\right)\mu\bar{\tau}}{\mu\bar{\tau}+\rho\left|\mathbf{v}\right|}\right)}, \quad \text{.....................(8)}$$

where k_{mr} is the relative minimum relative permeability, defined as the the ratio of minimum permeability to Darcy's permeability. $\nabla\Phi$ is the flow-potential gradient, as defined in Eq. 9:

$$\nabla\Phi = \left(\nabla P - \rho\ g\nabla D\right), \quad \text{.............................(9)}$$

where P is the pressure of the fluid, g is gravitational acceleration, and D is the depth from a datum.

Boundary and Initial Conditions. Boundary and initial conditions are needed to complete the mathematical description for non-Darcy flow in reservoirs. For single-phase flow, the initial status of the flow system is described by the initial condition or pressure spatial distribution. As with Darcy flow, there are three types of boundary conditions at wells or outer boundaries for non-Darcy flow: (1) first-type or Dirichlet boundary (i.e., constant or time-dependent pressure); (2) flux-type or Neuman boundary, depending on producing or injection condition; and (3) a more general third type of mixed pressure and flux boundary for multilayered well boundaries for general production or injection wells.

Numerical Formulation and Solution

The flow-governing equations, Eqs. 7 and 8, for single-phase non-Darcy flow of gas or liquid in porous media as described by the Barree and Conway model are highly nonlinear, and in general, need to be solved numerically. In this work, the methodology for using a numerical approach to simulate the non-Darcy flow consists of the following three steps: (1) spatial discretization of the mass-conservation equation; (2) time discretization; and (3) iterative approaches to solve the resulting nonlinear, discrete algebraic equations. A mass-conserving discretization scheme, based on control volume or integral finite difference (Pruess et al. 1999), is used and discussed here.

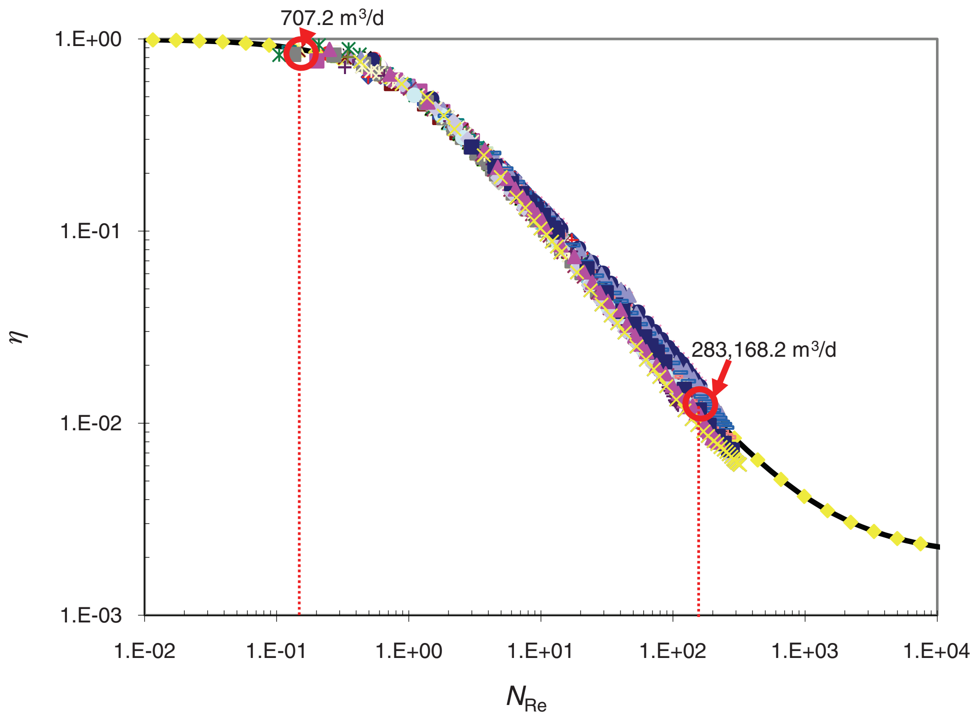

Fig. 4—Dimensionless plot of all tested proppants using the Barree and Conway model. As can be seen, all the experimental data collapse onto one curve that matches closely to the theoretical Barree and Conway model (shown as a dashed black and yellow line). One data plateau is clearly observed at low Reynolds numbers, and transition zones are captured. The test data cover field production rates from less than 707.2 m³/d to more than 283 168 m³/d.

The control-volume approach provides a general spatial discretization scheme that can represent a 1D, 2D, or 3D domain using a set of discrete meshes. Time discretization is carried out using a backward, first-order, fully implicit finite-difference scheme. Specifically, the non-Darcy-flow equations, as discussed previously, have been implemented into a three-phase reservoir simulator (Wu 2000, 2002). As implemented numerically, Eq. 7 is discretized in space using an integral finite-difference or control-volume scheme for a porous and/or fractured medium with an unstructured grid. The time discretization is carried out with a backward, first-order, finite-difference scheme. The discrete nonlinear equation for gas or liquid flow at Node i is shown in Eq. 10:

$$\left\{(\phi\rho)_i^{n+1}-(\phi\rho)_i^n\right\}\frac{V_i}{\Delta t}=\sum_{j\in\eta_i}\text{flow}_{ij}^{n+1}+Q_i^{n+1}, \quad \text{(10)}$$

where the superscript n denotes the previous time level, n+1 is the current time level, V_i is the volume of Element i (porous or fractured block), Δt is the timestep size, η_i contains the set of neighboring elements (j) (porous or fractured) to which Element i is directly connected, flow_{ij}^{n+1} is the mass "flow" term for the fluid between Elements i and j, and Q_i is the mass sink/source term at Element i for the fluid.

Based on the 1D flow rate, Eq. A-4, using the Barree and Conway model (Appendix A), the mass "flow" term (flow_{ij}^{n+1}) in Eq. 10 for the non-Darcy flow between Blocks i and j is evaluated by Eq. 11:

$$flow_{ij}=\frac{A_{ij}}{2\mu}\left[\begin{array}{l}-\left(\mu^2\bar{\tau}-\left(k_d k_{mr}\rho\right)_{ij+1/2}\left[\dfrac{\left(\Phi_j-\Phi_i\right)}{d_i+d_j}\right]\right)\\+\sqrt{\begin{array}{l}\left(\mu^2\bar{\tau}-\left(k_d k_{mr}\rho\right)_{ij+1/2}\left[\dfrac{\left(\Phi_j-\Phi_i\right)}{d_i+d_j}\right]\right)^2\\ \qquad +4\mu^2\left(\rho k_d\right)_{ij+1/2}\tau\left[\dfrac{\left(\Phi_j-\Phi_i\right)}{d_i+d_j}\right]\end{array}}\end{array}\right] \quad \text{(11)}$$

where the subscript ij+1/2 denotes a proper averaging or weighting of properties at the interface between the two Elements i and j, A_{ij} is the common interface area between the connected Blocks or Nodes i and j, d_i is the distance from the center of Block i to the common interface of Blocks i and j, and the flow-potential term in Eq. 11 is defined as in Eq. 12:

$$\Phi_i=P_i-\rho_{i\,j+1/2}\,g\,D_i. \quad \text{(12)}$$

Note that in Eq. 10, a discrete equation of mass conservation of the fluid has the same form regardless of the dimensionality of the model domain [i.e., it applies to 1D, 2D, or 3D analyses of flow through porous or fractured media (Wu 2002)].

Numerical-Solution Scheme. Eq. 10, the discrete nonlinear equation, is solved fully implicitly with a Newton-Raphson iteration method. Let us write the discrete nonlinear Eq. 10 in a residual form as Eq. 13:

$$R_i=\left\{(\phi\rho)_i^{n+1}-(\phi\rho)_i^n\right\}\frac{V_i}{\Delta t}-\sum_{j\in\eta_i}\text{flow}_{ij}^{n+1}-Q_i^{n+1}$$

$$(i = 1, 2, 3, \ldots, N), \quad \text{(13)}$$

where N is the total number of nodes/elements/gridblocks of the grid. Eq. 13 defines a set of (N) coupled nonlinear mass-balance equations that need to be solved simultaneously. In general, one primary variable per node is needed in the Newton iteration for solving one equation per node. We select fluid pressure as the primary variable, and treat all the rest of the dependent variables, such as viscosity, porosity, and density, as secondary variables, which are calculated from the primary variable at each node and at each iteration.

In terms of the primary variable, the residual equation, Eq. 13, at a Node i is regarded as a function of the primary variables not only at Node i, but also at all its directly neighboring nodes j. The Newton-Raphson iteration scheme leads to to Eq. 14:

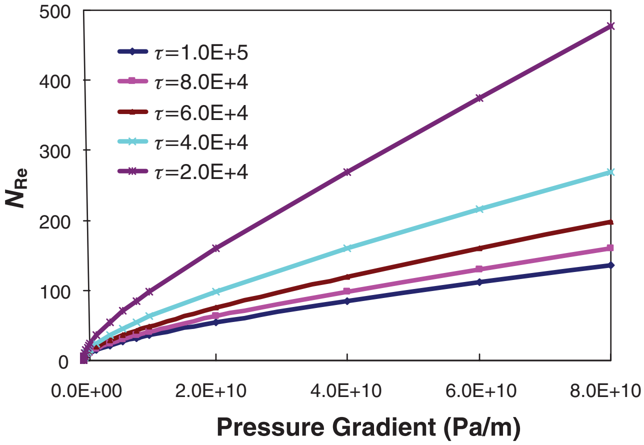

Fig. 5—Relationship between Reynolds number (N_{Re}) and pressure gradient (Pa/m) according to the Barree and Conway model. Relationships for different $\overline{\tau}$ values with k_{min} = 9.869E–10 m^2. The rest of the input parameters used are listed in Table 2.

$$\frac{\partial R_i^{n+1}\left(x_{j,p}\right)}{\partial x_j}\left(\delta x_{i,p+1}\right)=-R_i^{n+1}\left(x_{m,p}\right)$$

$$(i = 1, 2, 3, \ldots, N), \quad \text{.......................} (14)$$

where x_j is the primary variable at Node i and all its direct neighbors; p is the iteration level; and i =1, 2, 3, …, N. The primary variables in Eq. 14 need to be updated after each iteration, as shown by Eq. 15:

$$x_{p+1}=x_p+\delta x_{p+1}. \quad \text{.......................} (15)$$

The Newton-Raphson iteration process continues until the residuals, $R_i^{k,n+1}$, or changes in the primary variables, δx_{p+1}, over an iteration are reduced below preset convergence tolerances. In addition, the numerical method is used to construct the Jacobian matrix for Eq. 14, as outlined in Forsyth et al. (1995). At each Newton-Raphson iteration, Eq. 14 represents a system of N linearized algebraic equations with sparse matrices, which are solved by a linear iterative matrix-equation solver.

Treatment of Initial and Boundary Conditions. Dirichlet boundary conditions are handled with the "inactive cell" or "big-volume" method, as normally used in the TOUGH2 code (Pruess et al. 1999). In this method, a constant-pressure node is specified as an inactive cell or with a huge volume, while keeping all the other geometric properties of the mesh unchanged. For flux or Neuman boundary conditions, multilayered wells, and Cauchy or mixed boundary conditions, a general handling procedure is discussed in Wu et al. (1996) and Wu (2000).

Model Verification and Application

This section presents one verification and one application example to demonstrate the usefulness of the proposed numerical approach in modeling non-Darcy flow in reservoirs. First, we derive steady-state-flow analytical solutions and then use them to verify numerical-model results. The governing equation (Eq. 7) for 1D linear, horizontal, steady-state flow is simplified as Eq. 16:

$$\frac{\partial}{\partial x}(\rho v)=0. \quad \text{.......................} (16)$$

The flow rate according to the Barree and Conway model becomes:

$$v=\frac{-\left(\mu^2\overline{\tau}-k_d k_{mr}\rho\dfrac{\partial P}{\partial L}\right)+\sqrt{\left(\mu^2\overline{\tau}-k_d k_{mr}\rho\dfrac{\partial P}{\partial L}\right)^2+4\mu^2\rho k_d\overline{\tau}\dfrac{\partial P}{\partial L}}}{2\mu\rho}$$

$$\text{.......................} (17)$$

The solution for steady-state incompressible fluid flow is

$$P(x)=P_i-\frac{\mu\dfrac{\dot{m}}{A}\left(\dfrac{\dot{m}}{A}+\mu\overline{\tau}\right)(L-x)}{\left(\mu k_d\overline{\tau}+\dfrac{\dot{m}}{A}k_d k_{mr}\right)\rho_i}, \quad \text{.......................} (18)$$

and the solution for steady-state, slightly compressible fluid flow is

$$P=\frac{1}{c}\left(\begin{array}{l}-(1-cP_i)\pm\\ \sqrt{(1-cP_i)^2+2c\left[(1-\dfrac{c}{2}P_i)P_i+\dfrac{\mu\dfrac{\dot{m}}{A}\left(\dfrac{\dot{m}}{A}+\mu\overline{\tau}\right)(x-L)}{\left(\mu k_d\overline{\tau}+\dfrac{\dot{m}}{A}k_d k_{mr}\right)\rho_i}\right]}\end{array}\right)$$

$$\text{.......................} (19)$$

The detailed development of these two solutions, Eqs. 18 and 19, is provided in Appendix B.

Non-Darcy-Flow Behavior. Fig. 5 presents several characteristic curves of flow rate in terms of Reynolds number vs. pressure gradient according to the Barree and Conway model, and shows obvious nonlinear flow behavior. The plots in Fig. 5 are generated using Eq. 17 for 1D flow with the parameters given in **Table 2.** In examining the non-Darcy flow behavior between the curves of Fig. 5, we have found that the parameter $\overline{\tau}$ is more sensitive than other parameters for the normal range of pressure gradients. As the value of $\overline{\tau}$ decreases, the flow becomes more nonlinear, as shown in Fig. 5. In addition, **Fig. 6** shows the effect of the second Barree and Conway model parameter, k_{min}, on the flow rate vs. pressure gradient, showing the nonlinear behavior as k_{min} decreases.

Model Verification. Here, we use the analytical solution (Eq. 18) of 1D steady-state flow to check the numerical-simulation results. In numerical discretization, a 1D linear reservoir formation 10 m long, with a unit cross-sectional area, is represented by a 1D uniform linear grid of 1,000 elements with Δx = 0.01 m. The parameters used for this comparison are listed in **Table 3.** We compare two cases with different minimum-permeability and inverse-characteristic-length values, where Case 1 has k_{min} = 0.1 darcies and $\overline{\tau}$ = 100 000 (1/m) and Case 2 has k_{min} = 1.0 darcies and $\overline{\tau}$ = 10 000 (1/m). In the two scenarios, the pressure at the outlet boundary is maintained at 10^7 Pa, and a constant mass production rate is proposed at x = 0 for both the analytical and numerical solutions. The numerical calculation is carried out until steady state is reached.

TABLE 2—PARAMETERS USED IN FIGS. 5 AND 6 FOR PLOTTING RELATIONSHIPS BETWEEN FLOW RATE AND PRESSURE GRADIENT

Parameter	Value	Unit
Darcy permeability	k_d = 10	Darcy
Minimum permeability	k_{min} = 0.1	Darcy
Viscosity	μ = 0.001	Pa·s
Density	ρ =1,000	kg/m^3
Characteristic length	$\overline{\tau}$ =10,000–100,000	1/m

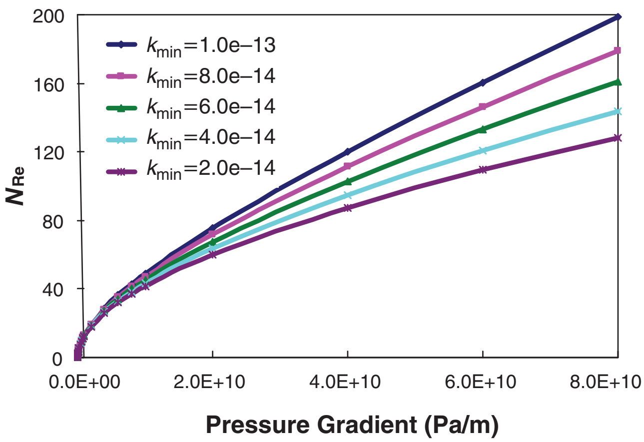

Fig. 6—Relationship between Reynolds number (N_{Re}) and pressure gradient (Pa/m) according to the Barree and Conway model. Relationships for different k_{min} values with $\overline{\tau}$ = 6.0e+04 m^{-1}. The rest of the input parameters used are listed in Table 2.

Fig. 7 shows the comparison results from the two solutions and indicates that excellent results are obtained from the numerical simulation, as compared to the analytical solution. Fig. 7 also shows that the pressure distributions for the two scenarios are linear along the linear-flow direction for the incompressible, steady-state flow cases. This is because the steady-state flow velocity is consistent everywhere; thus, the apparent permeability is also constant (Eq. 4), so we have a linear pressure profile.

Model Application. The application example presents a radial-flow problem using the numerical model to calculate transient pressure at an injection well. The reservoir formation is a uniform, radially infinite system (approximated by r_e = 10 000 000 m in the numerical model) of 10 m in thickness, and is represented by a 1D radial grid of 1,202 radial increments with a Δr size that increases logarithmically away from the well radius (r_w = 0.1 m). The formation is initially at a constant pressure of 10^7 Pa and is subjected to a constant volumetric-injection rate of 10 000 m^3/d at the well, starting at t = 0. Parameters used for the simulation study are listed in **Table 4.**

Fig. 8 presents the simulated transient-pressure responses at the well and a comparison for the four cases with a combination of minimum-permeability and characteristic-length values of Case 1 with Darcy flow (i.e., $k_{min} = k_d$); Case 2 with k_{min} = 0.1 darcies and $\overline{\tau}$ = 10 000 (1/m); Case 3 with k_{min} = 0.1 darcies and $\overline{\tau}$ = 100 000 (1/m); and Case 4 with k_{min} = 1 darcy and $\overline{\tau}$ = 10 000 (1/m). In Fig. 8, the lowest, solid, black curve shows the results for Case 1 (or Darcy flow) for comparison. The uppermost, solid-pink curve shows the results for Case 2, indicating the largest increase in injection pressure or the highest flow resistance caused by the non-Darcy flow because of the smaller values of the characteristic length $\overline{\tau}$ and minimum permeability k_{min}. The solid-blue-circle curve, the second from the bottom, is the result of Case 3, showing a very small difference from the Darcy-flow case because of using a large $\overline{\tau}$ (= 100 000). The green-triangle curve, the second from the top, is for Case 4, also showing a large injection-pressure increase because of a smaller $\overline{\tau}$ (= 10 000) used in this case.

It is very interesting to note that in all the four cases of Fig. 8, the pressure responses have a linear relationship with time on the semilog plot, except with the very early time. In addition, the four semilog straight lines are parallel to one another. This behavior indicates that (1) the impact of non-Darcy flow on pressure transients is equivalent to a constant flow resistance, superposed onto the pressure change of Darcy flow, and (2) the Darcy permeability k_d can be estimated using the slope of semilog straight lines from pressure-drawdown or -buildup curves.

Conclusions

Laboratory data from high-flow-rate tests through proppant packs show that the Barree and Conway model is able to describe the entire range of flow velocities from low to high flow rates under tests, while the Forchheimer model fails to cover the high end of flow rates. The experimental data set includes a matrix of proppant types and sizes and spans the range of gas-flow rates in most fields. In an effort to quantify non-Darcy-flow behavior in porous and fractured media and to complement the laboratory data, a mathematical/numerical model is developed by incorporating the Barree and Conway model into a general-purpose reservoir simulator. The numerical formulation for this inclusion is based on unstructured grids of control volume. In addition, several analytical solutions under steady-state linear-flow conditions are derived and used to verify the numerical-simulation results for the steady-state linear-flow case. These analytical solutions can be used to estimate non-Darcy flow-model parameters from laboratory data.

As an example of application, the numerical model is applied to evaluate the transient non-Darcy flow behavior at an injection well. The numerical-modeling results indicate that the parameter of inverse characteristic length $\overline{\tau}$ is more sensitive than other non-Darcy model parameters, while the impact of the minimum-permeability plateau is shown only at extremely large flow rates or pressure gradients. The analytical solutions and the numerical simulators from this work can be used for analyzing non-Darcy-flow behavior in laboratory, near-well flow, and field studies.

Nomenclature

A = cross-sectional area of flow, m^2
A_{ij} = common interface area between the connected Blocks or Nodes i and j
c = compressibility of porous media, 1/Pa
d_i = distance from the center of Block i to the common interface of Blocks i and j
D = depth from a datum
E = exponential constant, dimensionless

TABLE 3—PARAMETERS USED FOR MODE L VERIFICATION CHECKING NUMERICAL-SIMULATION RESULTS AGAINST THE ANALYTICAL SOLUTION, AS SHOWN IN FIG. 7

Parameter	Value	Unit
Cross section area	A = 1	m^2
Darcy permeability	k_d = 10	Darcy
Minimum permeability	k_{min} = 0.1, 1.0	Darcy
Viscosity	μ = 0.001	Pa·s
Characteristic length	$\overline{\tau}$ = 100,000, 10,000	1/m
Density	ρ =1,000	kg/m^3
Mass production rate	$\dot{m}$ = 5	kg/s
Pressure at outer boundary	P_i = 10^7	Pa

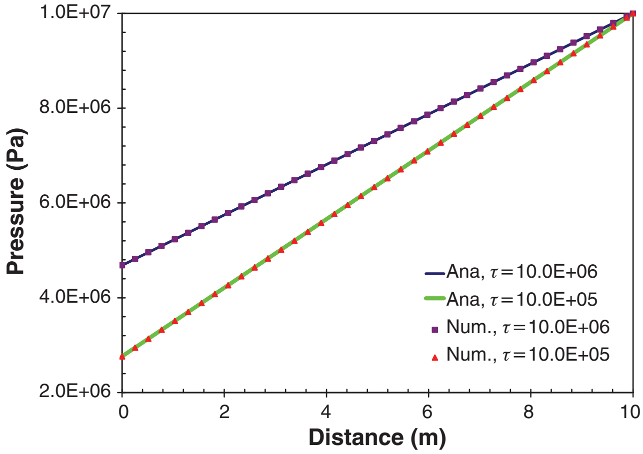

Fig. 7—Comparison between the analytical and numerical solutions for 1D steady-state flow in a linear system. The analytical solution for Case 1 is shown as a solid blue line, while the numerical solution for Case 1 is shown as purple squares. The analytical solution for Case 2 is shown as a solid green line, while the numerical solution for Case 2 is shown as red triangles. Model parameters used are listed in Table 3.

g = gravitational-acceleration constant
h = distance between each port, cm
k = permeability, darcies
k_{app} = apparent rate-dependent permeability, darcies
k_d = constant Darcy permeability, darcies
k_{min} = minimum permeability at high rate, darcies
k_{mr} = minimum permeability relative to Darcy permeability, fraction
L = length, m
$\dot{m}$ = fluid mass-flow rate, gm/sec
M = molecular gas weight
N = total number of nodes/elements/gridblocks of the grid
N_{Re} = Reynolds number, dimensionless
P_1 = pressure at Port 1, atm
P_2 = pressure at Port 2, atm
P_3 = pressure at Port 3, atm
P_4 = pressure at Port 4, atm
P_5 = pressure at Port 5, atm
P_i = initial pressure, Pa
P_{ti} = initial pressure in the gas tank, psig
P_{tf} = final pressure in the gas tank, psig
q = sink/source term

TABLE 4—PARAMETERS USED FOR SIMULATION OF TRANSIENT PRESSURE CHECKING NUMERICAL-SIMULATION RESULTS AGAINST THE ANALYTICAL SOLUTION, AS SHOWN IN FIG. 8

Parameter	Value	Unit
Darcy permeability	$k_d = 10$	Darcy
Minimum permeability	$k_{min} = 0.1, 1.0$	Darcy
Initial porosity	$\phi = 0.20$	
Viscosity	$\mu = 0.001$	Pa·s
Reference density	$\rho = 1{,}000$	kg/m^3
Volumetric injection rate	$q = 10{,}000$	m^3/d
Total compressibility of fluid and rock	$C_T = 6.0\times10^{-10}$	1/Pa
Well radius	$r_w = 0.1$	M
Formation thickness	$h = 10$	M
Initial-formation-gas pressure	$P_i = 10^7$	Pa

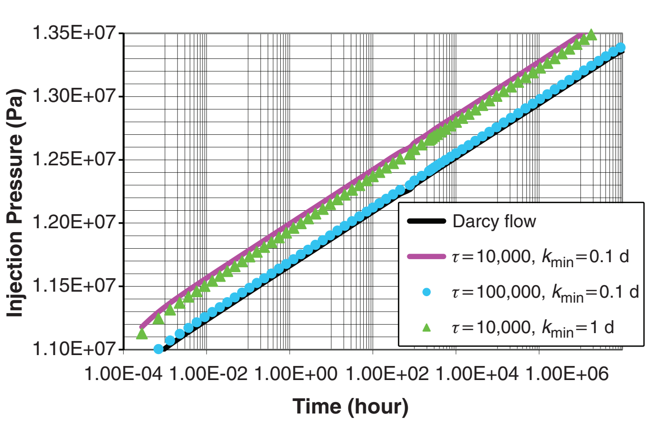

Fig. 8—Transient-pressure responses simulated at an injection well. Case 1 gives the bottom black solid curve for Darcy flow (i.e., $k_{min} = k_d$); Case 2 gives the top solid pink curve, [i.e., k_{min} = 0.1 darcies and $\bar{\tau}$ = 10 000 (1/m)]; Case 3 gives the solid-blue-circle curve [i.e., k_{min} = 0.1 darcies and $\bar{\tau}$ = 100 000 (1/m)]; and Case 4 gives the solid-green-triangle curve [i.e., k_{min} = 1 darcy and $\bar{\tau}$ = 10 000 (1/m)]. The simulation parameters used are listed in Table 4.

Q = fluid volumetric-flow rate, m^3/s
Q_i = mass sink/source term at Element i for the fluid
r = radius distance, m
r_s = skin-zone radius, m
r_w = wellbore radius, m
R = gas universal constant
T = temperature, K
T_{ti} = initial temperature in the gas tank, °F
T_{tf} = final temperature in the gas tank, °F
v = superficial velocity, m/s
V_i = volume of Element i
z = gas z-factor
$\partial P/\partial L$ = potential gradient, Pa/m
β = non-Darcy coefficient, 1/m or 1/cm
Δt = timestep size
μ = fluid viscosity, poise or Pa.s
ρ = fluid density, kg/m^3
ρ_i = initial density, kg/m^3
$\bar{\tau}$ = inverse of the characteristic length, 10 000/ m
ϕ = effective porosity of the medium
$\nabla\Phi$ = flow-potential gradient

Acknowledgments

The authors wish to thank the members of the Fracturing, Acidizing, Stimulation Technology (FAST) Consortium located at the Colorado School of Mines and the Stimlab Proppant Consortium for their support. Yu-Shu Wu would also like to thank the support from Sinopec Inc. of China through the National Basic Research Program of China (2006CB202400).

References

Barree, R.D. and Conway, M.W. 2004. Beyond Beta Factors: A Complete Model for Darcy, Forchheimer, and Trans-Forchheimer Flow in Porous Media. Paper SPE 89325 presented at the SPE Annual Technical Conference and Exhibition, Houston, 26–29 September. http://dx.doi.org/10.2118/89325-MS.

Carmen, P.C. 1937. Fluid Flow Through Granular Beds. *Trans. Inst. Chem. Engrs. London* **15:** 150–166.

Darcy, H.P.G. 1856. *The Public Fountains of the City of Dijon (Les Fontaines publiques de la ville de Dijon)*, trans. P. Bobeck. Dubuque, Iowa: Kendall Hunt Publishing Co. (1 March 2004). ISBN 0-7575-0540-6. http://biosystems.okstate.edu/darcy/FountainsTranslation.htm.

Ergun, S. 1952. Fluid Flow Through Packed Columns. *Chem. Eng. Prog.* **48** (2): 89–94.

Fand, R.M., Kim, B.Y.K, Lam, A.C.C., and Phan, R.T. 1987. Resistance to the Flow of Fluids Through Simple and Complex Porous Media Whose Matrices Are Composed of Randomly Packed Spheres. *J. Fluids Eng.* **109:** 268–274.

Forchheimer, P.F. 1901. Wasserbewegung durch Boden. *Zeitschrift des Vereines deutscher Ingenieure* **45** (5): 1781–1788.

Forsyth, P.A., Wu, Y.S., and Pruess, K. 1995. Robust numerical methods for saturated-unsaturated flow with dry initial conditions in heterogeneous media. *Adv. Water Resour.* **18** (1): 25–38. http://dx.doi.org/10.1016/0309-1708(95)00020-J.

Griffiths, D.V. and Smith, I.M. 2006. *Numerical Methods for Engineers*, second edition. Boca Raton, Florida: Chapman and Hall/CRC.

Jones, S.C. 1972. A Rapid Accurate Unsteady-State Klinkenberg Permeameter. *SPE J.* **12** (5): 383–397. SPE-3535-PA. http://dx.doi.org/10.2118/3535-PA.

Kececioglu, I. and Jiang, Y. 1994. Flow Through Porous Media of Packed Spheres Saturated With Water. Transactions of ASME 116: 164. *J. Fluids Eng.* **116** (1): 164–170. http://dx.doi.org/10.1115/1.2910229.

Lai, B.T. 2010. Experimental Measurement and Numerical Modeling of High Velocity Non-Darcy Flow Effects in Porous Media. PhD dissertation, Colorado School of Mines, Golden, Colorado.

Lopez. H.D. 2007. Experimental Analysis and Macroscopic and Pore-level Flow Simulations to Compare Non-Darcy Flow Models in Porous Media. PhD dissertation, Colorado School of Mines, Golden, Colorado.

Martins, J.P., Milton-Tayler, D., and Leung, H.K. 1990. The effects of Non-Dardy Flow in Propped Hydraulic Fractures. Paper SPE 20709 presented at the SPE Annual Technical Conference and Exhibition, New Orleans, 23–26 September. http://dx.doi.org/10.2118/20709-MS.

Montillet, A. 2004. Flow Through a Finite Packed Bed of Spheres: A Note on the Limit of Applicability of the Forchheimer-Type Equation. *J. Fluids Eng.* **126** (1): 139. http://dx.doi.org/10.1115/1.1637928.

Pruess, K., Oldenburg, C., and Moridis, G. 1999. TOUGH2 User's Guide, Version 2.0. Report LBNL-43134, Contract No. DE-AC03-76SF00098, Lawrence Berkeley National Laboratory, Berkeley, Calforina (November 1999).

Wu, Y.-S. 2000. A virtual node method for handling wellbore boundary conditions in modeling multiphase flow in porous and fractured media. *Water Resour. Res.* **36** (3): 807–814. http://dx.doi.org/10.1029/1999WR900336.

Wu, Y.-S. 2002. Numerical Simulation of Single-Phase and Multiphase Non-Darcy Flow in Porous and Fractured Reservoirs. *Transport in Porous Media* **49** (2): 209–240. http://dx.doi.org/10.1023/A:101601802018.

Wu, Y.-S., Forsyth, P.A., and Jiang, H. 1996. A consistent approach for applying numerical boundary conditions for subsurface flow. *J. Contam. Hydrol.* **23** (3): 157–185. http://dx.doi.org/10.1016/0169-7722(95)00099-2.

Appendix A—Relationship of Flow Rate vs. Pressure Gradient With the Barree and Conway Model

The flow rate of 1D linear flow with the Barree and Conway equation (Barree and Conway 2004) for fluid velocity is derived and provided in Eqs. A-1 through A-4.

$$\frac{\partial P}{\partial x}=\frac{\mu v}{k_d\left(k_{mr}+\dfrac{1-k_{mr}}{1+\dfrac{\rho v}{\mu \overline{\tau}}}\right)}. \qquad \text{(A-1)}$$

This is simply a modified Eq. A-1:

$$\frac{\partial P}{\partial x}=\frac{\mu v}{k_d\left(\dfrac{k_{mr}\mu\tau+k_{mr}\rho v+\mu\tau-k_{mr}\mu\tau}{\mu\tau+\rho v}\right)}. \qquad \text{(A-2)}$$

Writing Eq. A-2 in a quadrautic form gives

$$\mu\rho v^2+\left(\mu^2\tau-k_d k_{mr}\rho\frac{\partial P}{\partial x}\right)v-k_d\mu\tau\frac{\partial P}{\partial x}=0. \qquad \text{(A-3)}$$

Solving for v in Eq. A-3, we obtain

$$v=\frac{-\left(\mu^2\overline{\tau}-k_d k_{mr}\rho\dfrac{\partial P}{\partial x}\right)+\sqrt{\left(\mu^2\overline{\tau}-k_d k_{mr}\rho\dfrac{\partial P}{\partial x}\right)^2+4\mu^2\rho k_d\overline{\tau}\dfrac{\partial P}{\partial x}}}{2\mu\rho} \qquad \text{(A-4)}$$

Note that Eq. A-2 is applicable to both incompressible and compressible fluid flow, according to the Barree and Conway model.

Appendix B—Steady-State-Flow Solutions for Incompressible and Slightly Compressible Liquids and Gas

We consider 1D, steady-state, non-Darcy flow in a linear porous medium according to the Barree and Conway model. The governing equation is

$$\frac{\partial}{\partial x}(\rho v)=0. \qquad \text{(B-1)}$$

The linear-flow system with a length of L and cross-sectional area A is subject to (1) constant mass flux $\dot{m}$ and (2) constant pressure ($P = P_i$) at the outlet, $x = L$. A solution of Eq. B-1 with the two conditions is

$$\rho\frac{-\left(\mu^2\overline{\tau}-k_d k_{mr}\rho\dfrac{\partial P}{\partial x}\right)+\sqrt{\left(\mu^2\overline{\tau}-k_d k_{mr}\rho\dfrac{\partial P}{\partial x}\right)^2+4\mu^2\rho k_d\overline{\tau}\dfrac{\partial P}{\partial x}}}{2\mu\rho}=\frac{\dot{m}}{A} \qquad \text{(B-2)}$$

Eq. B-2 can be further simplified as

$$\left(\mu k_d\overline{\tau}+\frac{\dot{m}}{A}k_d k_{mr}\right)\rho\frac{\partial P}{\partial x}=\mu\frac{\dot{m}}{A}\left(\frac{\dot{m}}{A}+\mu\overline{\tau}\right). \qquad \text{(B-3)}$$

Note that Eq. B-3 is a general solution and is applicable for both liquid and gas flow according to the Barree and Conway non-Darcy model.

Incompressible Fluid-Flow Solution. For incompressible single-phase liquid ($\rho = \rho_i$), integrating Eq. B-3 and using the boundary condition at $x = L$, we obtain

$$\left(\mu k_d\overline{\tau}+\frac{\dot{m}}{A}k_d k_{mr}\right)\rho_i P=\mu\frac{\dot{m}}{A}\left(\frac{\dot{m}}{A}+\mu\overline{\tau}\right)x+\left(\mu k_d\overline{\tau}+\frac{\dot{m}}{A}k_d k_{mr}\right)\rho_i P_i-\mu\frac{\dot{m}}{A}\left(\frac{\dot{m}}{A}+\mu\overline{\tau}\right)L$$

and Eq. 18.

Slightly Compressible Fluid-Flow Solution. For slightly compressible single-phase liquid flow,

$$\rho \approx \rho_i[1+c(P-P_i)]. \quad \text{(B-4)}$$

Substituting Eq. B-4 for Eq. B-3 and completing the integration, we have the solution (Eq. 19) for slightly compressible fluid flow.

Gas-Flow Solution. For single-phase gas flow, the density is described by the real-gas law

$$\rho = \frac{PM}{zRT}. \quad \text{(B-5)}$$

Substituting Eq. B-5 into Eq. B-2 and performing the integration leads to

$$\left(\mu k_d \bar{\tau} + \frac{\dot{m}}{A} k_d k_{mr}\right) \int_{P_i}^{P} \frac{PM}{zRT} \mathrm{d}P = \mu \frac{\dot{m}}{A}\left(\frac{\dot{m}}{A} + \mu \bar{\tau}\right) \int_0^x \mathrm{d}x. \quad \text{(B-6)}$$

Then, the steady-state-flow solution for single-phase gas is given by

$$\left(\mu k_d \bar{\tau} + \frac{\dot{m}}{A} k_d k_{mr}\right) \frac{M}{RT} \int_{P_i}^{P} \frac{P}{z} \mathrm{d}P = \mu \frac{\dot{m}}{A}\left(\frac{\dot{m}}{A} + \mu \bar{\tau}\right) x. \quad \text{(B-7)}$$

Bitao Lai is an assistant professor in the Petroleum Engineering Department at the University of Louisiana at Lafayette in Lafayette, Louisiana. She has more than 8 years of laboratory research experience and teaches a variety of courses, including phase behavior, reservoir engineering, and petroleum economics. Her research interests include reservoir characterization, reservoir rock mechanics, and multiphase flow in porous media. Lai holds an MS degree in geotechnical engineering and a PhD degree in petroleum engineering. She serves as a reviewer for SPE journals and *Petroleum Science and Engineering.*

Jennifer L. Miskimins is an associate professor in the Petroleum Engineering Department at the Colorado School of Mines (CSM) in Golden, Colorado. Miskimins is the founder and Director of the Fracturing, Acidizing, Stimulation Technology (FAST) Consortium at CSM. She teaches a variety of courses including completions and stimulation classes, geologic field camps, and petroleum economics. Miskimins holds BS, MS, and PhD degrees in petroleum engineering. She served as the Executive Editor for the *SPE Production & Operations* Journal from 2008–2011 and was a 2010–2011 SPE Distinguished Lecturer.

Yu-Shu Wu is a professor and CMG Reservoir Modeling Chair in Petroleum Engineering at CSM. He is also a guest scientist at the Earth Sciences Division of the Lawrence Berkeley National Laboratory. At CSM, he teaches reservoir engineering courses, supervises graduate students, and conducts research in the areas of multiphase fluid and heat flow in porous media, enhanced oil recovery (EOR) operation, CO_2 geosequestration, reservoir simulation, enhanced geothermal systems, and unconventional hydrocarbon reservoirs. He holds BS and MS degrees in petroleum engineering from universities in China, and MS and PhD degrees in reservoir engineering from the University of California at Berkeley. He serves as an Associate Editor for *SPE Journal.*